Journal of Alloys and Compounds 845 (2020) 156307

Contents lists available at ScienceDirect

Journal of Alloys and Compounds

journal homepage: http://www.elsevier.com/locate/jalcom

Structural, vibrational and electronic properties in the glass-crystal transition of thin films $Sb_{70}Te_{30}$ doped with Sn

V. Bilovol [a, b, *], M. Fontana [a, b], J.A. Rocca [a, b], H.H. Medina Chanduví [d], A.M. Mudarra Navarro [d], A.V. Gil Rebaza [d], L.A. Errico [d, e], A. Liang [c], D. Errandonea [c], A.M. Ureña [a, b]

[a] *Universidad de Buenos Aires, Facultad de Ingeniería, Laboratorio de Sólidos Amorfos, Av. Paseo Colón 850, C1063ACV, Buenos Aires, Argentina*
[b] *CONICET, Universidad de Buenos Aires, Instituto de Tecnologías y Ciencias de la Ingeniería "Hilario Fernández Long" (INTECIN), Av. Paseo Colón 850, C1063ACV, Buenos Aires, Argentina*
[c] *Departamento de Física Aplicada-ICMUV, Universidad de Valencia, MALTA Consolider Team, Edificio de Investigación, C/Dr. Moliner 50, 46100, Burjassot, Valencia, Spain*
[d] *Instituto de Física La Plata IFLP-CONICET, CCT-La Plata, Departamento de Física, Facultad de Ciencias Exactas de la Universidad Nacional de La Plata UNLP, 1900, La Plata, Argentina*
[e] *Universidad Nacional del Noroeste de la Provincia de Buenos Aires, UNNOBA, Monteagudo 2772, CP 2700, Pergamino, Buenos Aires, Argentina*

ARTICLE INFO

Article history:
Received 27 April 2020
Received in revised form
2 July 2020
Accepted 4 July 2020
Available online 7 July 2020

Keywords:
Chalcogenide glasses
Non-volatile memories
Raman spectroscopy
DFT

ABSTRACT

Antimony-telluride based phase-change materials doped with Sn have been proposed to be ideal materials for improving the performance of phase-change memories. It is well known that $Sb_{70}Te_{30}$ thin films show a sharp fall in the electrical resistance in a narrow temperature range when heating. Therefore, it is interesting to study the effect of adding Sn into this composition. In this work, undoped and Sn-doped Sb—Te thin films of composition $Sn_x[Sb_{0.70}Te_{0.30}]_{100-x}$, with x = 0.0, 2.5, 5.0 and 7.5 at. %, have been obtained by pulsed laser deposition. Their electrical resistance has been measured while heating from room temperature to 650 K. A sharp fall in the electrical resistance, associated to the glass-crystal transition, has been detected in all the samples within a narrow temperature range. The onset temperature of this transformation increases with the Sn content. Both as-obtained and thermally-treated films have been structurally characterized by X-ray and by Raman spectroscopy. We have compared the results among these compositions in terms of the identified crystallization products, transformation onset temperatures, transformation temperature ranges and amorphous/crystallized electrical resistance ratio. We have found that the frequency of the Raman modes decreases with Sn-doping. Finally, in order to study the electronic structure and to determine the band gap, the frequencies of the allowed Raman modes and the vibration directions of the $Sb_{70}Te_{30}$ compound, Density Functional Theory based *ab initio* calculations have been performed as a function of the Sn concentration.
© 2020 Elsevier B.V. All rights reserved.

1. Introduction

The big data era requires real-time processing of huge amounts of information and hence generating a need for new computing technologies. In this concern phase change materials (PCM) are the most promising candidates for application in the emerging non-volatile memory technologies. These memories meet many requirements: they are fast, scalable, and present low power consumption [1–3].

Non-volatile PCMs for data storage devices are usually chalcogenide-based, that is, they contain one of the following elements from VI group of the periodic table: S, Se, Te. Particularly, PCM alloys obtained as thin films exhibit exceptional physical properties: fast and reversible phase transformations (switching) between crystalline and amorphous states. In consequence optical and electrical properties in these states are remarkably different [4,5]. The amorphous phase exhibits a high electrical resistivity, in a contrast to the crystalline phase, characterized by an essentially lower resistivity. These outstanding properties underlie the distinct

* Corresponding author. Universidad de Buenos Aires, Facultad de Ingeniería, Laboratorio de Sólidos Amorfos, Av. Paseo Colón 850, C1063ACV, Buenos Aires, Argentina.
E-mail address: vbilovol@fi.uba.ar (V. Bilovol).

https://doi.org/10.1016/j.jallcom.2020.156307
0925-8388/© 2020 Elsevier B.V. All rights reserved.

approach used for the (new) emerged data storage technology. The introduction of metallic impurity atoms such as aluminum, copper, silver or tin in the chalcogenide glasses is expected to improve the performance of the PCM-based memories. It has already been shown the addition of Sn into $Ge_2Sb_2Te_5$ improved some crucial parameters of the compound [6]. Understanding structural particularity, especially, tin place in the host matrix, is the key parameter to understand the improved electrical (optical) performance.

Recently, $Sn_x(Sb_{0.70}Te_{0.30})_{100-x}$ (with x = 0, 2.5, 5.0 and 7.5 at. %) as-cast alloys have been characterized by X-ray diffraction (XRD) and Mössbauer spectroscopy. We have found that $Sb_{70}Te_{30}$ crystallizes in a trigonal structure which is described by space group *P-3m1*. The crystal structure is schematically shown in Fig. 1. On the other hand, doping with Sn leads to structural distortions of the unit cell that can be described, for all the Sn concentrations, with the *C2/m* space group [7]. The *C2/m* structure for ternary samples $Sn_x(Sb_{0.70}Te_{0.30})_{100-x}$ is a slight distortion of the *P-3m1* binary structure. The hyperfine parameters of Mössbauer spectroscopy indicate that tin behaves as Sn^{2+} (occupying Sb1 site) and ratifies that has a slightly distorted environment.

In this work thin films of compositions $Sn_x(Sb_{0.70}Te_{0.30})_{100-x}$ (with x = 0, 2.5, 5.0 and 7.5 at. %) have been obtained by pulsed laser deposition (PLD). Their structural and electrical behaviors with the temperature have been studied to analyze the amorphous-crystal transformation emphasizing the features provided by Raman spectroscopy and *ab initio* calculations. Also, the electronic structure and the band gap of both pure and Sn-doped $Sb_{70}Te_{30}$ have been discussed.

2. Methodology

2.1. Experimental

$Sn_x(Sb_{0.70}Te_{0.30})_{100-x}$ thin films (with x = 0.0, 2.5, 5.0 and 7.5 at. %) have been prepared by pulsed laser deposition (PLD) from bulk chalcogenide targets with specified compositions. Bulk samples have been first prepared by direct synthesis from pure elements (4 N) [8]. Stoichiometric proportions of the reactants have been loaded into 10 mm diameter quartz tubes. The loaded tubes have been evacuated to $3 \cdot 10^{-5}$ mbar and sealed. The batches have been heated in a furnace at 800 °C for 8 h. Melts have been slowly cooled down to room temperature inside the ampoules. After this process, samples have been sliced and polished to obtain PLD targets with parallel faces.

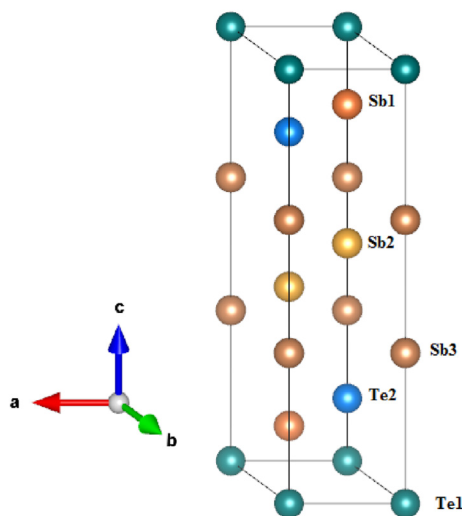

Fig. 1. Crystal structure of $Sb_{70}Te_{30}$ with space group *P-3m1*. The three distinguished crystallographic sites for Sb atoms (Sb1, Sb2 and Sb3) and two crystallographic sites for Te atoms (Te1 and Te2) are shown with different colors. (For interpretation of the references to color in this figure legend, the reader is referred to the Web version of this article.)

Thin films have been deposited on static substrates (chemically cleaned microscope glass slides) held at room temperature, which have been parallelly aligned to the target surface, inside a vacuum chamber. PLD has been performed using a pulsed Nd:YAG laser (Spectra-Physics Quanta-Ray Lab-150) with deposition times of 30–40 min, operating at a 355 nm wavelength, with a 5 ns pulse duration and a 10 Hz repetition rate. The laser beam with a 45° angle of incidence has been horizontally spanned by moving a mirror in order to get uniform ablation of the target surface. The energy density of the laser spot has been 1.1–1.3 J/cm^2. The chemical composition of as-obtained films has been performed by Energy Dispersive X-Ray technique using Oxford Instruments X-MaxN 50SDD joint to JSM-6510LV (Jeol) scanning microscope. All analyses of the as-obtained films confirmed the nominal composition sample within an error limit of 2–4 at. %.

Electrical resistance has been measured on the surface of the deposited films, using a two-point probe over sputtered Pt-contacts, in coplanar configuration separated by a length *L*, connected to a low-current/high-resistance electrometer. Films have been placed in a vacuum cell (evacuated to 10^{-2} mbar with rotary pump) and heated by a resistance furnace from room temperature to 650 K, with a heating rate of 5 K/min.

As-deposited and thermally treated films have been analyzed by X-ray diffraction in the grazing incidence geometry with a grazing angle $\omega = 0.5°$. Smartlab Rigaku diffractometer with a monochromatized Cu-K$_\alpha$ radiation has been used measuring at 0.05° step and sweeping with a 0.16°/min.

Vibrational characterization has been performed by Raman spectroscopy using a LabRAM HR Raman system (Horiba Jobin Yvon), equipped with a confocal microscope and a charge coupled device detector. A 1.800 gr/mm grating and 100 μm hole results in a 2 cm^{-1} spectral resolution. The 514.5 nm line of an Ar$^+$ laser has been used as the excitation source.

2.2. Computational details

As we have mentioned in the Introduction, $Sb_{70}Te_{30}$ crystallizes in a trigonal *P-3m1* space group structure, while the doping with Sn leads to structural distortions of the unit cell, which can be described by the *C2/m* space group [7]. In both cases, there are three different crystallographic sites for Sb atoms (Sb1, Sb2 and Sb3) and two crystallographic sites for Te atoms (Te1 and Te2). We also demonstrated in ref. [7] that Sn dopants preferably replace Sb atoms of type 1 (Sb1) of the $Sb_{70}Te_{30}$ structure (Fig. 1). Based on these results we will focus the discussion on the *C/2 m* phase and only the case of Sn atom replacing for Sb1 has been considered. In order to study the Sn-doped system, $Sn_x(Sb_{0.70}Te_{0.30})_{100-x}$, as a function of the Sn concentration *x*, we have employed different supercells of dimensions $2a \times 1b \times 3c$, $1a \times 1a \times 3c$, and $1a \times 1b \times 2c$ sizes with the *C2/m* crystal structure. In each supercell a single Sb1 has been replaced by a Sn one and structural and electronic distortions induced by the impurity in the host lattice have been computed. For these supercells we obtained molar Sn-concentrations of 2.78, 5.56 and 8.33 at. %, respectively. Details of the structure (lattice parameters, atomic positions) can be found in Ref. [7].

All *ab initio* calculations have been performed in the framework of the Density Functional Theory (DFT) [9], where the self-consistent Kohn-Sham equations have been solved using the pseudopotential and plane-wave method, implemented in the

Quantum-Espresso code [10]. The exchange-correlation (XC) potential has been described using the Perdew-Burke-Ernzerhof (PBE) parametrization of the Generalized Gradient Approximation (GGA) [11]. Ionic cores of the Sb, Te and Sn atoms have been described using Ultrasoft pseudopotential from the Standard Solid State Pseudopotential Library (SSSP) [12]. The converged kinetic energy cutoff for the wave-function and charge density have been 90 Ry and 900 Ry, respectively. All lattice vectors and atomic positions have been optimized performing variable-cell relax calculations, where the convergence criteria have been forced on each atom smaller than 10^{-5} Ry/Bohr and the residual stress on cell less than 0.1 kbar. The reciprocal space has been described using a dense mesh-grid of 11x11x5 *k*-points to sample the Brillouin zone.

Vibrational properties have been calculated using the density functional perturbation theory (DFPT) [13], implemented in the Quantum-Espresso code [10]. Only Gamma point (Γ) [14] has been considered, where the dynamic matrix and frequencies of the phonon modes have been computed using DFPT linear response method.

The electronic structure of pure and Sn-doped $Sb_{70}Te_{30}$ have been studied using the Full-Potential Linearized Augmented Plane-Wave (FP-LAPW) as implemented in the Wien2k code [15]. The muffin-tin radii used have been $R_{MT}(Te) = 1.16$ Å, $R_{MT}(Sb) = 1.06$ Å, and $R_{MT}(Sn) = 1.06$ Å, whereas the parameter related with the basic-set size has been set to $R_{MT}xK_{max} = 8$ (R_{MT} is the smallest muffin-tin and K_{max} is related with the plane wave cut-off). For the description of the XC potential and the reciprocal space the same approximations and *k*-points mesh detailed above were used. In order to improve the calculation of the electronic band-gap we have also used Trna-Blaha modified Becke-Jhonson (TB-mBJ) exchange potential [16–18].

3. Results and discussion

3.1. Thermic evolution of the electrical resistance and X-ray diffraction

Thin film electrical resistance (*R*) of samples with compositions $Sn_x(Sb_{0.70}Te_{0.30})_{100-x}$ (with $x = 0.0$, 2.5, 5.0 and 7.5 at. %) evolves upon heating as shown in Fig. 2. Each *R(T)* plot (normalized to its room temperature value) shows one sharp transition where the value of resistance falls several orders of magnitude in a small temperature range. These transitions are associated with structural changes [19]: the amorphous phase of the as-obtained thin films evolves to a crystalline phase.

All the phases, before and after the sharp transition, show a semiconducting behavior. The electric resistance decreases with temperature, as can be seen in Fig. 2. Therefore, temperature dependence of resistance can be written as the Arrhenius-type equation:

$$R(T) = L\Big/(e.w.\sigma_0)\exp\left(\frac{E_a}{kT}\right) \quad (1)$$

where E_a is the apparent activation energy, k is the Boltzmann's constant, σ_0 the conductivity pre-exponential factor, w and L are the width and the length between contacts and e is the film thickness. E_a values are obtained linearizing equation (1). Fig. 3 shows ln(R) vs 1/T plots for each composition. Arrhenius plots on temperature dependence of resistance show different regions with the characteristic activation energies for the amorphous and crystalline states. Linear dependence of ln(R) as $1/T$ for both amorphous and crystalline phases suggests a thermally activated conduction mechanism. Thermal and electrical parameters in the glass-to-crystal transitions for $Sn_x(Sb_{0.70}Te_{0.30})_{100-x}$ are gathered in Table 1.

The electrical resistance of thin films exhibits a remarkable contrast (~MΩ – ~kΩ) when measured before and after the thermal treatments due to glass - crystal transition. As it has been aforementioned, this result is an excellent property of phase-change materials. The value of the ratio amorphous state to crystalline state resistances *Rg/Rc* for the studied alloys is about $3\text{–}4\times10^2$. These values are in very good agreement with the expected values for materials that have applications in PCM-based memories [20].

The onset temperatures T_{on} for the glass-crystal transition in $Sb_{70}Te_{30}$ thin films are in accordance with previous works [21,22] observing a difference of about 20 K. The values of ratio T_{on}/T_m (ratio of crystallization to melt temperature) are about 0.48–0.49. This is a good property for applications in PCM-based memories. We notice that onset temperature of the glass-crystal transition increases with the tin content (Fig. 4 (a)). Similar behaviors are reported when Ag, Al, Cu, Ga, Ge, W or Zn has been added to $Sb_{0.70+y}Te_{0.30-y}$ ($0 \le y \le 0.12$) [23–28].

Table 1 shows the dependence of the glass activation energy for

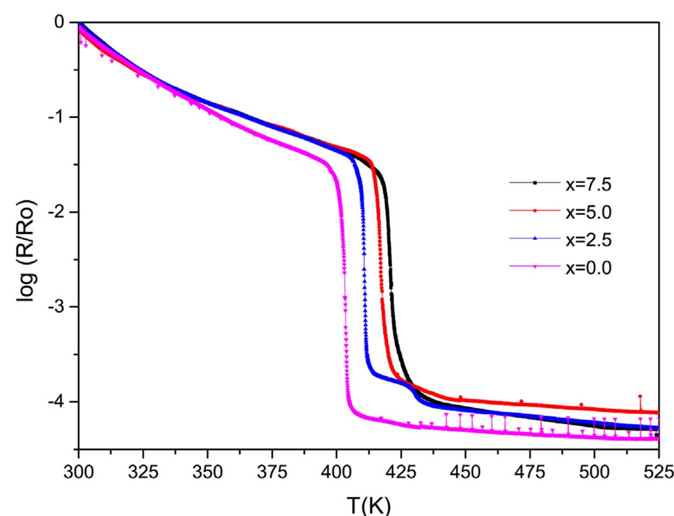

Fig. 2. Temperature dependence of normalized electrical resistance for the $Sn_x(Sb_{0.70}Te_{0.30})_{100-x}$ ($x = 0.0$, 2.5, 5.0 and 7.5 at. %) thin films.

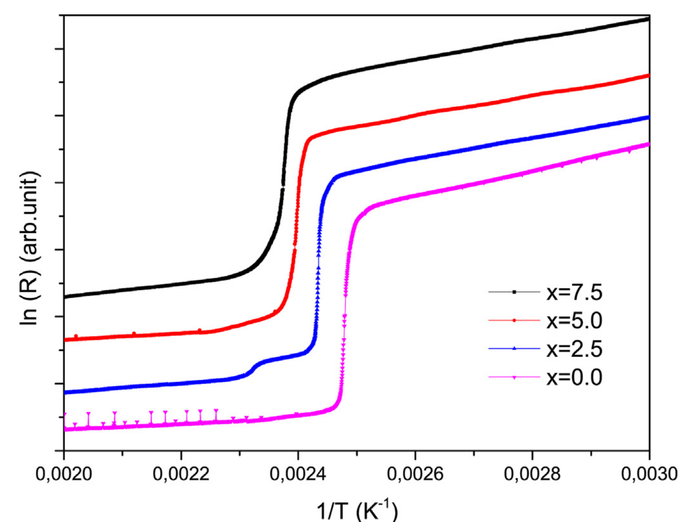

Fig. 3. Electrical resistance vs. $1/T$ for the $Sn_x(Sb_{0.70}Te_{0.30})_{100-x}$ (with $x = 0.0$, 2.5, 5.0 and 7.5 at. %) thin films. Data corresponding to $x = 2.5$, 5.0 and 7.5 have been displaced on the vertical axis for clarity.

Table 1
Thermal and electric parameters of $Sn_x(Sb_{0.70}Te_{0.30})_{100-x}$ (with $x = 0.0$, 2.5, 5.0 and 7.5 at. %). Temperatures have been determined for the transitions glass – crystal (T_{on}). E_{a1} and E_{a2} are the activation energies for the glass and crystal. The melting temperature T_m has been estimated using the corresponding phase diagrams [30]. R_g and R_c are the resistance of the glass and the crystal.

x (%)	T_{on} (K) ±2	E_{a1}(eV/at) Glass	E_{a2}(eV/at) Crystalline	T_m (K) ±5	T_{on}/T_m	R_g/R_m
0.0	396	0.35 ± 0.01	0.06 ± 0.01	823	0.48	4.2×10^2
2.5	403	0.31 ± 0.03	0.12 ± 0.02	828	0.48	4.1×10^2
5.0	410	0.28 ± 0.01	0.08 ± 0.01	833	0.49	2.8×10^2
7.5	413	0.30 ± 0.02	0.17 ± 0.02	843	0.49	3.0×10^2

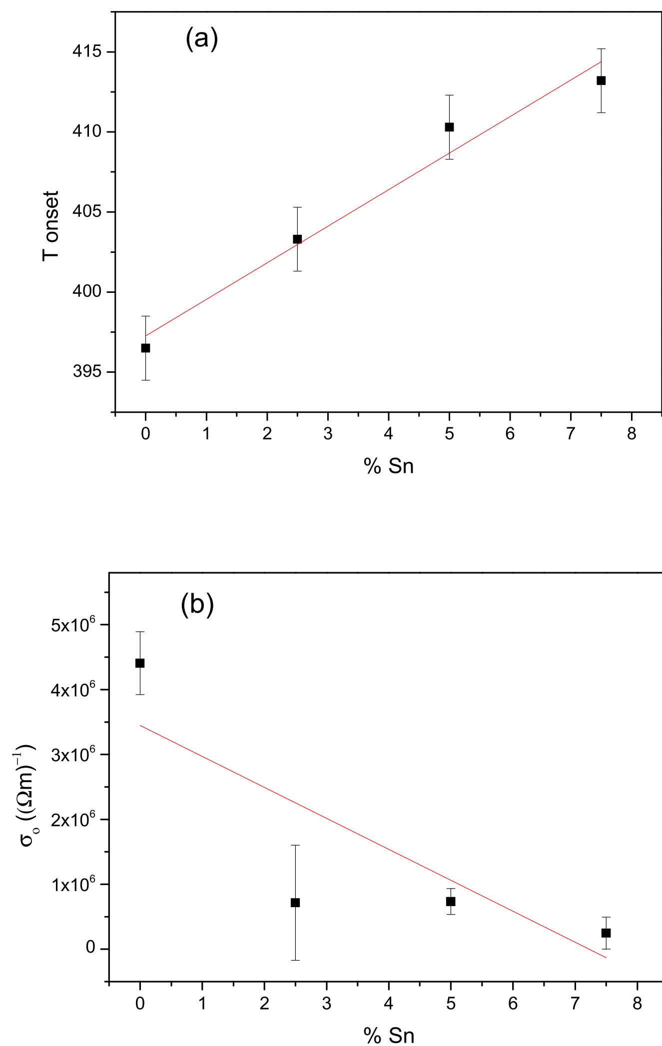

Fig. 4. (a) Onset temperature of the glass-crystal transition *vs* tin content, (b) Pre-exponential conductivity factor in the Arrhenius equation (Eq. (1)) *vs* tin content.

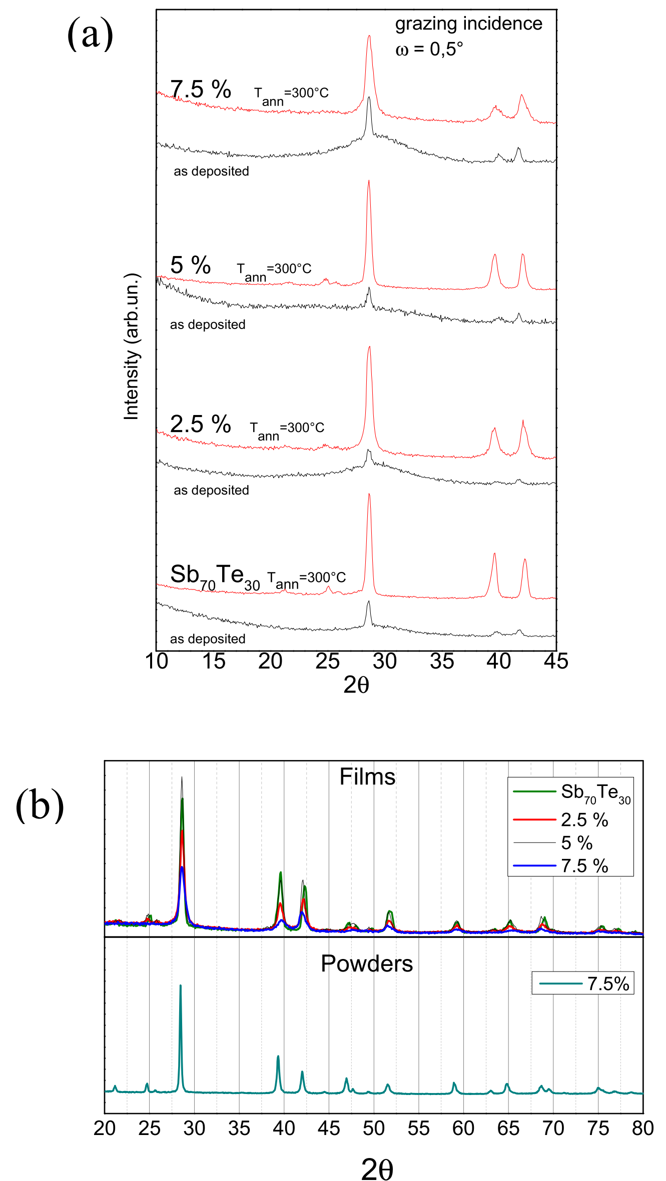

Fig. 5. a) X-ray diffractograms of $Sn_x(Sb_{0.70}Te_{0.30})_{100-x}$ as-deposited and thermally treated films in a short 2θ range. b) X-ray diffractograms of $(Sb_{0.70}Te_{0.30})_{100-x}Sn_x$ thermally treated films in a long 2θ range (top) and powdered target with x = 7.5 at. % (bottom) of C2/*m* space group shown as reference one [7].

electrical conduction with x, observing that tin adding does not change significantly the activation energy of the glass. As a rule, in amorphous chalcogenides, the following dependence is held: $E_a = E_{opt}/2$ [29]. That is, the optical band gap (E_{opt}) is two times the activation energy of electrical conductivity. Based on this, the band gap is nearly 0.60 eV independently from Sn concentration.

On the other hand, the conductivity pre-exponential factor (σ_0) decreases almost linearly with tin concentration (Fig. 4 (b)). Such a behavior indicates an increase in the localized density of states. The last fact is in accordance with ref. [23], where $Sb_{70}Te_{30}$ has been doped with Ge.

The behavior of band-gap and σ_0 with increasing Sn content could suggest that Sn is acting as an impurity center in the amorphous state of the films.

X-ray diffractograms of both as-deposited and thermally treated films are displayed in Fig. 5a (shown in a short 2θ range). X-ray

patterns of the PLD as-obtained films are characteristic of an amorphous phase with traces of a crystalline phase. After the thermal treatment, the films become crystalline as it can be appreciated from the patterns shown in a long 2θ range (Fig. 5b (top)). Previously, when studying powder samples with the same nominal composition, we showed [7] that the increasing of tin content in the $Sb_{70}Te_{30}$ compound lead to the progressive distortion of the crystal structure, favoring a second-order transition from the reference trigonal structure (space group P-*3m1*) to a monoclinic structure (space group *C2/m*). As it could be expected, thermally treated thin films grown by PLD from targets with the corresponding compositions revealed same trend as their parent powders. Here we display as well the XRD pattern of powders with x = 7.5 at. % already shown in ref. [7] for the comparison purposes (Fig. 5b (bottom)).

Comparing structural parameters extracted from the experimental XRD patterns of the films (Table 2) and powders with the corresponding nominal composition (see Table 1 in Ref. [7]), the same trends are observed. In both cases, the addition of tin leads to an increase of the *a* and *b* unit-cell lattice parameters, in contrast with a decrease observed for the *c* parameter.

3.2. Raman spectroscopy

In Fig. 6 we present the results obtained from Raman spectrometry measurements. As-deposited amorphous films show a broad peak at 144-145 cm^{-1}. The frequency of this broad peak is independent of the sample composition and has a full-width at half maximum of 35–38 cm^{-1}. The results obtained for each composition are given in Table 3. The observed Raman mode is related to the vibration of amorphous Sb–Te bonds [24]. The broadening of the associated peak is associated to the disorder present in the amorphous films [31]. After the thermal treatment, in all the samples we found that the broad band is transformed into five well defined Raman modes (see Fig. 6). This is consistent with the recrystallization observed in XRD measurements.

We will now discuss the assignment of the modes observed in the crystalline thin films. Since the doped and un-doped samples have very similar Raman spectra, and the crystal structure of the doped samples is a slight distortion of the structure of the undoped sample, for the sake of simplicity, we will base the discussion upon the assignment of the modes of the un-doped sample (space group *P-3m1*) made from our DFT calculations. Group theory predicts 18 phonons for $Sb_{70}Te_{30}$ being the mechanical representation at the Γ point of the Brillouin zone: $\Gamma = 4A_{1g} + 5A_{2u} + 5E_u + 4E_g$, one A_{2u} and one E_u are the acoustic modes. The optical modes can be divided as infrared-active modes: $4A_{2u} + 4E_u$ and Raman active modes: $4A_{1g} + 4E_g$.

The DFT-based *ab initio* calculations of the phonons at the Γ–point of the Brillouin zone have been performed considering the *P-3m1* and *C2/m* crystal structures to describe the $Sb_{70}Te_{30}$ compound. For the case of the *C2/m* crystal structure, we have found some imaginaries values of the phonon frequencies, whereas for the *P-3m1* crystal structure all phonon frequencies are positive. This result indicates that the *C2/m* crystal structure is not stable for undoped $Sb_{70}Te_{30}$ [32], in agreement with the results reported for the formation energy, which show that the *P-3m1* structure is the one with the lowest free energy [7].

For the case of the $Sb_{70}Te_{30}$ compound with the *P-3m1* space group, we have obtained eighteen different phonons belonging to Infrared (I) and Raman (R) actives modes. As we have previously mentioned the optical modes have the assignment $\Gamma = 4A_{1g} + 5A_{2u} + 5E_u + 4E_g$. In Table 4, we report the calculated wave-length of all the phonons for the different symmetries.

In the experiments we observed a total of five Raman modes. From these modes, four can be correlated with vibrations of $Sb_{70}Te_{30}$ according with DFT calculations (see Table 4). These are the modes we observed at 98.1, 127.4, 141.1, and 158.4 cm^{-1}, which can be assigned to two 2 A_{1g} and two E_g, with frequencies 104.2 cm^{-1} (E_g), 133.2 cm^{-1} (E_g), 155.8 cm^{-1} (A_{1g}), and 161.0 cm^{-1} (A_{1g}) according to calculations. The other four modes are predicted to be at frequencies lower than 62 cm^{-1}, which is below the lowest frequency that can be measured by our Raman set-up. Notice the excellent agreement between the theoretical and experimental results.

Calculations, in addition of helping with the mode assignment, provide information of the atomic movements associated to each vibration. These movements are obtained by means of the eigenvectors of each mode. In Fig. 7, we show the main components of the eigenvectors for the atomic displacements for each phonon corresponding to the Raman modes of the $Sb_{70}Te_{30}$ compound with *P-3m1* space group that match with experimental data. The length of the arrows is related with the magnitude of the displacement. These theoretical Raman modes are in good agreement with our experimental data. For the case of the wavelength of 161.0 cm^{-1}, it is related with notorious displacement of the atoms Sb2 and Sb3, almost parallel to the c-axis, but in opposite ways. The wavelength of 155.8 cm^{-1} is related mainly with the displacement of Sb1 and Te2 atoms, almost parallel to the c-axis, but in opposite ways. The wavelength of 133.2 cm^{-1} is related with the displacement of the Sb2 and Sb3 atoms in opposite ways but perpendicular to the *c*-axis. Finally, the wavelength of 104.2 cm^{-1} is related with the displacement of the Sb1 and Te2 atoms perpendicular to the *c*-axis but in opposite ways. As usual, the highest frequency mode corresponds to a stretching vibration and the other modes to bending vibrations. We also observed that in-plane vibrations (those perpendicular to c-axis) are the lowest frequency observed modes. This is consistent with the fact that due to the "layered" crystal structure of $Sb_{70}Te_{30}$ movements within the layers (a-b plane) requests less energy than out-of-plane vibrations.

The fifth mode observed in the experiments (and not assigned to $Sb_{0.70}Te_{0.30}$) is at 110.1 cm^{-1} in the un-doped simple. This mode can be correlated with the A_1 mode of Te, which suggests the presence of an excess of Te. Interestingly, the frequency of this mode is the least affected by the incorporation of Sn, which supports the hypothesis that this mode is not inherent to the studied samples but caused by the presence of an excess of Te. Regarding the influence of Sn in the other modes, we have noticed that all of them move to lower frequencies as Sn concentration increases. This is consistent with a weakening of bonds which suggests that local bonding is influenced by the incorporation of Sn [7]. In particular, the most intense peak is at 158 cm^{-1} and moves to 152 cm^{-1} as Sn concentration increases. The second most intense peak is at 127 cm^{-1} and moves to 120 cm^{-1}. This behavior compares well with the one observed in Zn-doped samples [24]. The softening of modes under the incorporation of Sn might be related with a mechanical instability of the crystal structure of $Sb_{70}Te_{30}$ when large concentrations of Sn are incorporated [33]. This is consistent with the formation of a rhombohedral layered structure (space group *R-3m*) when more than 10 at.% of Sn is incorporated into $Sb_{70}Te_{30}$ [34].

Table 2
Calculated unit-cell parameters (*a*,*b* and *c*) using X-ray diffractograms.

x (%)	Space Group	a (Å)	b (Å)	c (Å)	β (degree)	γ (degree)
0.0	P-3m1	4.282	4.282	17.314	90.00	120
2.5	C2/m	7.426	4.287	17.288	90.08	90
5.0	C2/m	7.439	4.293	17.260	90.11	90
7.5	C2/m	7.441	4.300	17.175	90.14	90

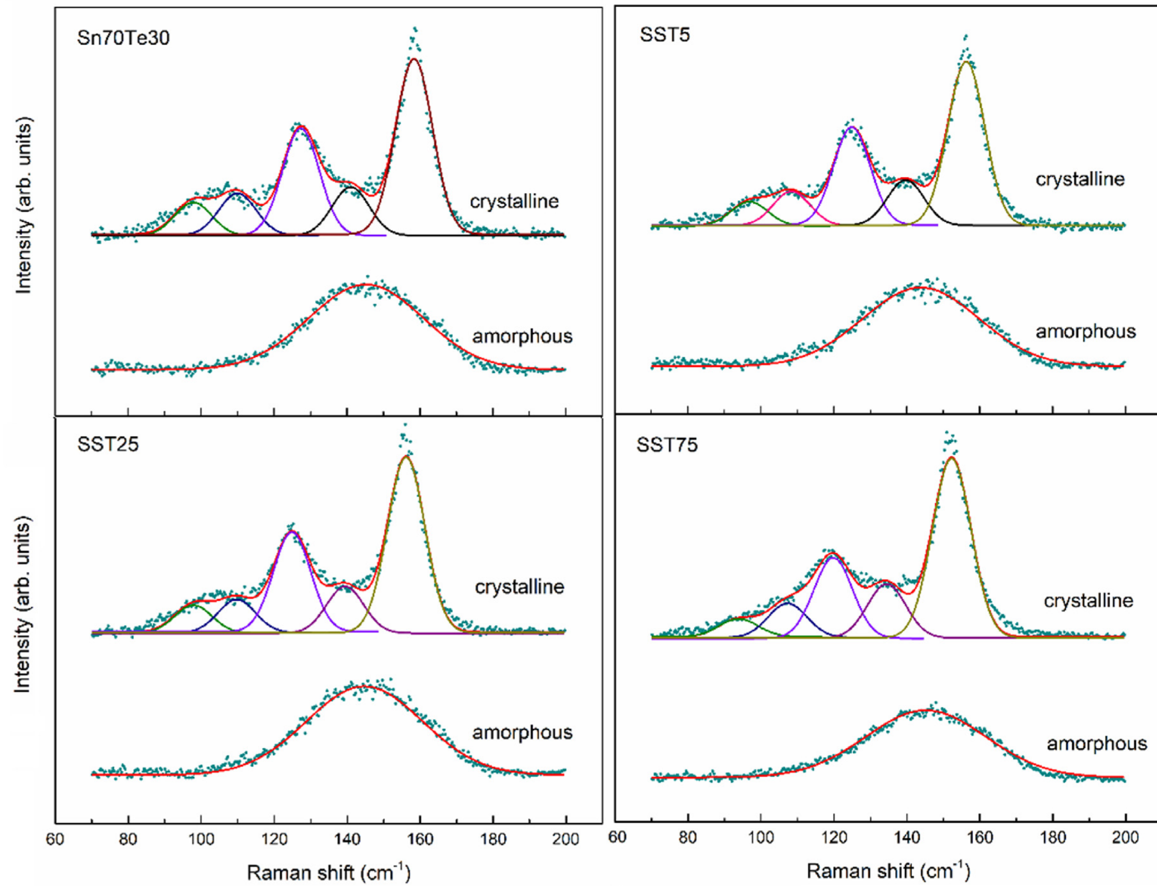

Fig. 6. Raman spectra of the different samples in the amorphous and crystalline form. Compositions are indicated in the figures.

Table 3
The fitted results of the experimental Raman spectra.

x (%)	Thin film condition		Peak 1	Peak 2	Peak 3	Peak 4	Peak 5
0.0	as-obtained	position	145.41				
		FWHM	36				
	thermally treated	position	98.121	110.08	127.39	141.1	158.42
		FWHM	11.88	11.88	11.88	11.88	11.88
5.0	as-obtained	position	144.15				
		FWHM	35.61				
	thermally treated	position	96.505	108.25	124.9	139.67	156.31
		FWHM	11.81	11.81	11.81	11.81	11.81
2.5	as-obtained	position	144.87				
		FWHM	35.16				
	thermally treated	position	96.930	109.11	124.77	139.33	156.15
		FWHM	12.15	12.15	12.15	12.15	12.15
7.5	as-obtained	position	145.17				
		FWHM	38.75				
	thermally treated	position	94.756	107.88	119.95	134.53	152.28
		FWHM	12.32	12.32	12.32	12.32	12.32

Table 4
Phonon wavelengths calculated using DFPT for the crystal structure with space group *P-3m1* of $Sb_{70}Te_{30}$. We highlight in bold letters the phonons measured in the experiments. I: infrared R: Raman.

Symmetry	Phonon wave-length (cm^{-1})				
E_u	1.8 (I)	22.0 (I)	76.6 (I)	95.2 (I)	145.6 (I)
A_{2u}	3.2 (I)	30.0 (I)	106.8 (I)	140.5 (I)	163.2 (I)
E_g	37.3 (R)	44.9 (R)	**104.2 (R)**	**133.2 (R)**	
A_{1u}	49.5 (R)	61.2 (R)	**155.8 (R)**	**161.0 (R)**	

3.3. Electronic structure and band gap

In order to analyze the changes induced by the Sn-impurities in the electronic structure of $Sb_{70}Te_{30}$ we have calculated the density of state (DOS) of the pure compound. In all cases both the GGA and the TB-mBJ functionals predict a direct band gap of about 0.08 − 0.1 eV (see Fig. 8) as expected for this kind of materials for applications in PCM devices. Fig. 8 also shows the local DOS projected onto the Sb and Te atoms. The total DOS is composed of two valence bands: a lower narrow band lying at about 9 − 10 eV below the

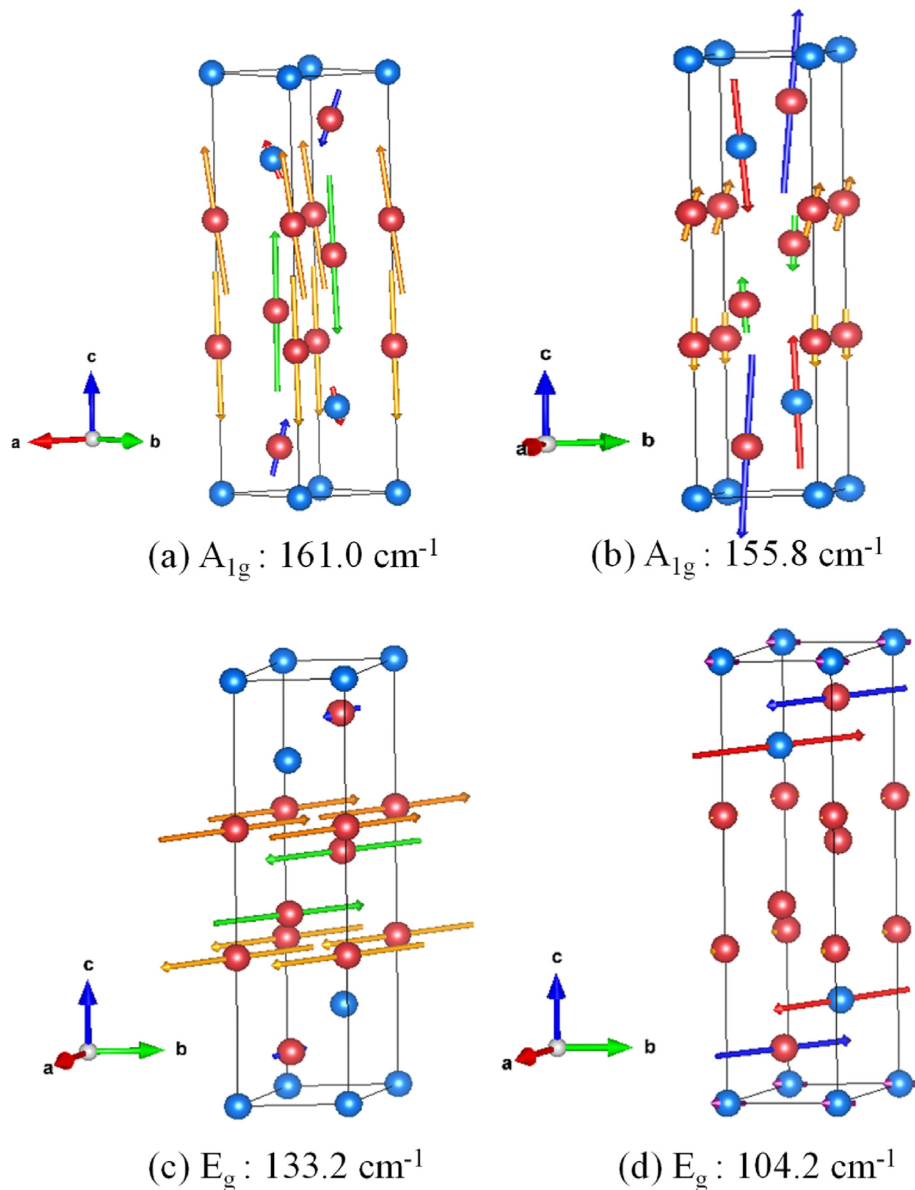

Fig. 7. $Sb_{70}Te_{30}$ unit cell. Atomic displacements belong to the active Raman modes. For the symmetry A_{1g}: (a) and (b), and symmetry E_g: (c) and (d). Blue and red spheres represent Te and Sb atoms, respectively. (For interpretation of the references to color in this figure legend, the reader is referred to the Web version of this article.)

Fermi level composed mainly by Sb and Te 5*s* states and an upper band between - 6.0 and 0.0 eV that has mainly Sb and Te 5*p* character. The conduction band is a mixture of mainly Sb and Te 5*p* orbitals.

Now we can focus our study on the electronic structure of the Sn-doped $Sb_{70}Te_{30}$ compounds. The results correspond to the *C2/m* structure considering that Sn atoms substitute Sb1 atoms [7]. At this point we must discuss a crucial point in the calculation of the electronic structure of a doped semiconductor system: the charge state of the impurity [35]. Based on a Bader analysis [36] we found that the charges in the muffin-tin spheres of Sb and Sn atoms are 47.77*e* and 48.21*e*, respectively. In the framework of a pure ionic model this corresponds to Sn and Sb atoms acting with 2+ and 3+ oxidation states. When a Sn^{2+} atom replaces a Sb^{3+} atom in the supercell the resulting system is metallic due to the lack of one electron necessary to fill up the valence band (see Fig. 9 for the case of a Sn concentration of 5.56 at. %. Similar results have been obtained for 2.78 and 8.33 at. % Sn concentrations). Comparison of Figs. 8 and 9 shows that the presence of the Sn impurity in the semiconductor introduces the appearance of a Sn-*s* band (in the energy ranging from - 8 to - 6 eV) and an acceptor impurity state at the top of the valence band in the corresponding DOS, that can be better seen looking at the inset of Fig. 9. The impurity states are spatially located at Sn and at their Te nearest-neighbour atoms.

The question that arises here is if the real system we want to describe provides the lacking electron to fill the acceptor impurity level located at the Fermi energy via defects or simply by a thermal effect. In the framework of a rigid band model, if we fill the acceptor impurity level, the system recovers the semiconductor nature (in agreement with the experimental results) with a band gap of about $0.2 - 0.3$ eV depending on the Sn concentration.

To better describe the situation and to consider the filling of impurity level in a self-consistent way we have performed calculations adding one electron to the whole system. As can be seen by comparing the results presented in Figs. 9 and 10 ($Sb_{70}Te_{30}$ doped with a 5.56 at. % of Sn) the electronic band gap is 0.33 eV. The same

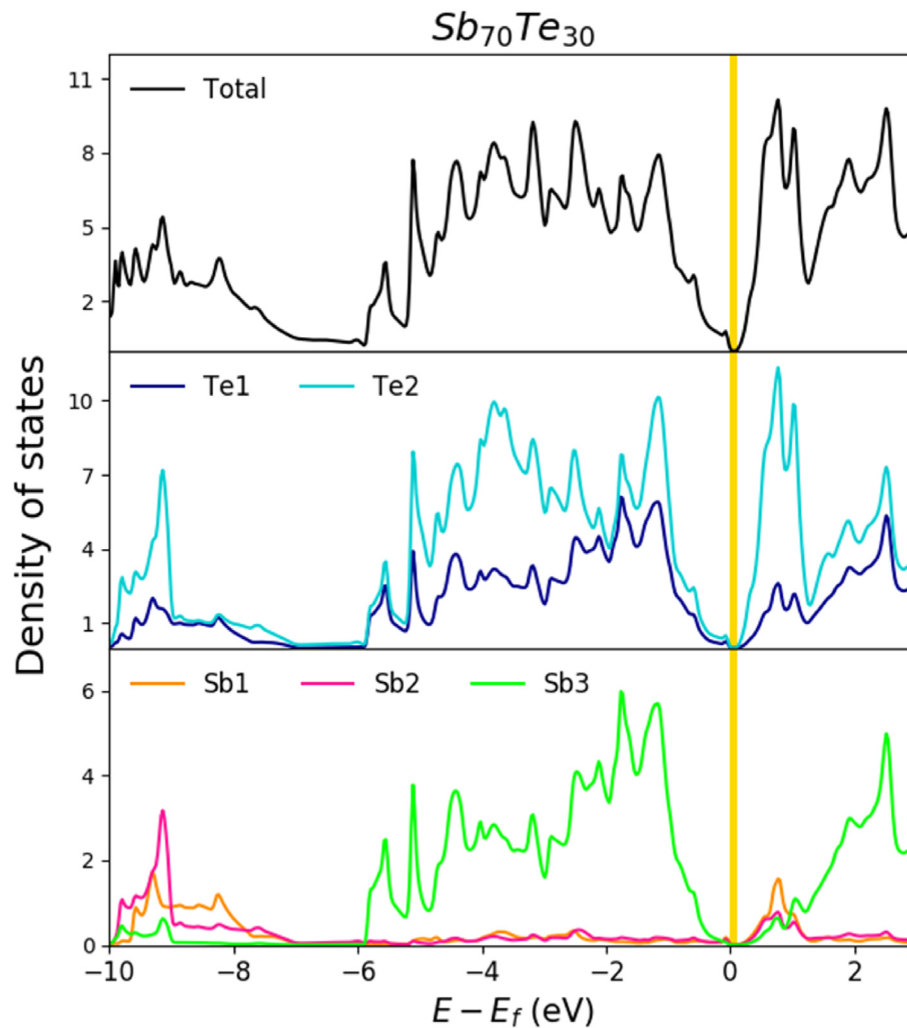

Fig. 8. Density of states (DOS) for the un-doped $Sb_{70}Te_{30}$ compound, and the corresponding contribution of the different Sb (Sb1, Sb2, and Sb3) and Te (Te1 and Te2) atoms.

behavior has been found for 2.78 and 8.33 at. % Sn concentrations.

Going further with the electronic structure analysis, in Fig. 11 we present the electronic band dispersion curves for a reciprocal path (through principal symmetric points) for the Sn-doped $Sb_{70}Te_{30}$ (5.56 at. % Sn concentration and semiconductor case) in order to determine if the electronic band gap is direct or indirect. For all doped cases, we have found that electronic band gap is direct and takes place at the symmetric $\Gamma-$point of the reciprocal space.

Here, we would like to make some reasonings about the band gaps. As it is mentioned in section 3.1, we have estimated the optical band gap in the amorphous state through the experimentally determined activation energy reported in Table 1. It is nearly 0.60 eV independently from Sn concentration. The fact that the electronic band gap in the crystalline state is direct, it is approximately equal to the optical band gap in the crystalline state. It was calculated to be around 0.33 eV, independently from Sn content. The optical band gap is typically larger in the amorphous state than in the crystalline one for PCMs [37]. Therefore, considering this fact, the results of our *ab initio* calculations do not contradict the experimental ones. In addition, the experimental and simulated data are consistent with respect to the dependence on the composition, showing that the optical band energy does not depend on the Sn content.

4. Conclusions

In this work we have experimentally and theoretically studied the structural, vibrational, and electronic properties and the glass-crystal transition of pure and Sn-doped Sb–Te thin films of composition $Sn_x[Sb_{0.70}Te_{0.30}]_{100-x}$, with $x = 0.0, 2.5, 5.0$ and 7.5 at. %.

The thin films have been obtained by pulsed laser deposition. Both as-obtained and thermally-treated films have been characterized by X-ray and by Raman spectroscopy. The thermally-treated films show the same crystalline structure as their parent powders with the same corresponding compositions. As it has been previously showed $Sb_{70}Te_{30}$ crystallizes in a trigonal *P-3m1* space group structure while doping with Sn leads to structural distortions of the unit cell, which can be described by monoclinic *C2/m* space group.

The electrical resistance of the samples has been measured while heating from room temperature to 650 K. A sharp fall in the electrical resistance has been experimentally detected and associated to the glass-crystal transition. This change in the resistivity of the samples has been detected in a narrow temperature range and the glass-crystal transition temperature continuously increases with the incorporation of Sn dopants. From the analysis of our date we have found that the parameters T_{on}/T_m and R_g/R_c of the studied films show good values for the application in non-volatile

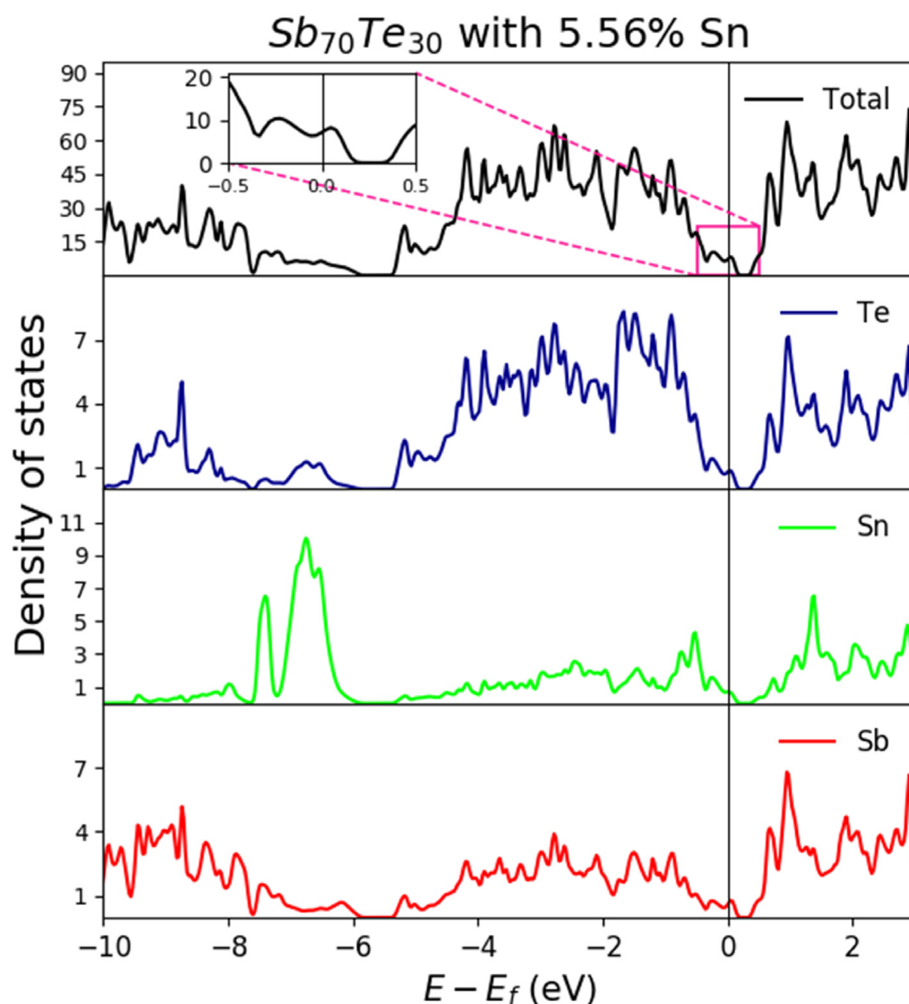

Fig. 9. Density of states (DOS) for $Sb_{70}Te_{30}$ doped with 5.56 at. % of Sn. Inset: Zoom in a range of energy around the Fermi energy showing the different description of the system after adding an electron.

memories.

Raman experiments have showed that the as-deposited amorphous films revealed a broad peak at 144-145 cm^{-1}, independently of the sample composition. The observed Raman mode is related to the vibration of amorphous Sb—Te bonds and the broadening of the peak has been associated to the disorder of the amorphous films. After the annealing treatment (during *R vs T* measurements) the broad band is transformed into five well defined Raman modes as a result of crystallization process. The A_{1g} and E_g Raman vibrational modes associated with Sb_2Te_3 slabs have been identified. A red shift with Sn content due to the change of the bond distances caused by lattice distortion induced by the Sn impurities was registered. The DFT-based *ab initio* calculations allowed identifying the measured Raman modes as: a stretching Sb—Sb vibration along the c-axis that corresponds to the highest frequency A_{1g} mode, an Sb—Te bending vibration along the c-axis for the other A_{1g} mode, an in-plane Sb—Te bending vibration perpendicular to the c-axis for the lowest frequency E_g mode, and a Sb—Sb in-plane scissoring vibration perpendicular to the c-axis for the other E_g mode.

Going to the electronic structure of pure and Sn-doped $Sb_{70}Te_{30}$ our *ab initio* calculations find that $Sb_{70}Te_{30}$ (when crystallized) presents a semiconductor nature, with a narrow direct band gap in the order of 0.1 eV. The presence of the Sn dopants induces an acceptor impurity level in the electronic band-structure of $Sb_{70}Te_{30}$. The comparison experiment-theory enables us to determine that this impurity level is fully occupied at room temperature. In this situation, the doped system (when crystallized) is a semiconductor with a direct band gap in the order of 0.3 eV and nearly independent of the Sn-concentration. The simulated and the experimental results are consistent.

CRediT authorship contribution statement

V. Bilovol: Conceptualization, Supervision, Writing - original draft, Writing - review & editing, Formal analysis, Investigation. **M. Fontana:** Conceptualization, Formal analysis, Writing - original draft, Writing - review & editing, Visualization. **J.A. Rocca:** Investigation, Validation, Software. **H.H. Medina Chanduví:** Formal analysis. **A.M. Mudarra Navarro:** Formal analysis. **A.V. Gil Rebaza:** Writing - original draft, Writing - review & editing, Visualization, Formal analysis. **L.A. Errico:** Writing - original draft, Writing - review & editing, Formal analysis. **A. Liang:** Visualization, Formal analysis. **D. Errandonea:** Writing - original draft, Writing - review & editing, Formal analysis. **A.M. Ureña:** Investigation, Resources, Funding acquisition.

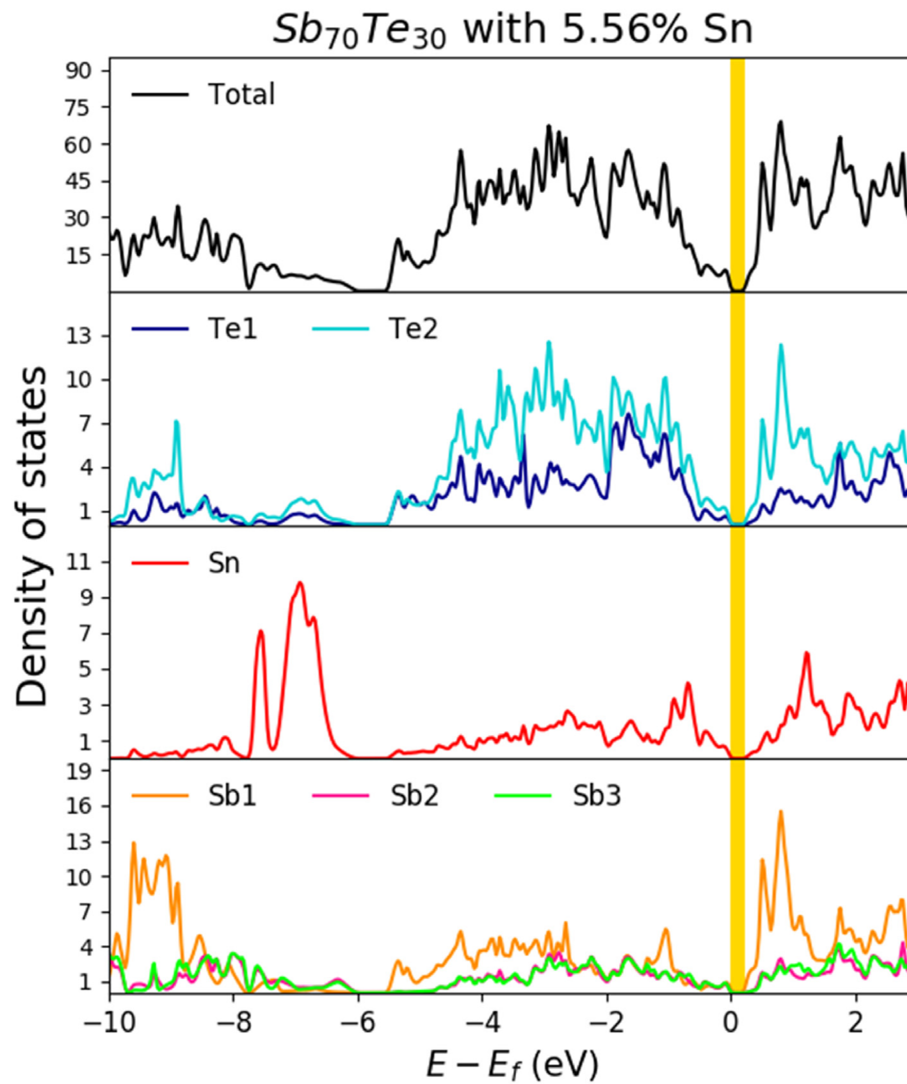

Fig. 10. Density of state (DOS) for the 5.56 at. % Sn-doped $Sb_{70}Te_{30}$ charged system, and the corresponding contribution of each atom. The band gap of the system is represented with the yellow bar. (For interpretation of the references to color in this figure legend, the reader is referred to the Web version of this article.)

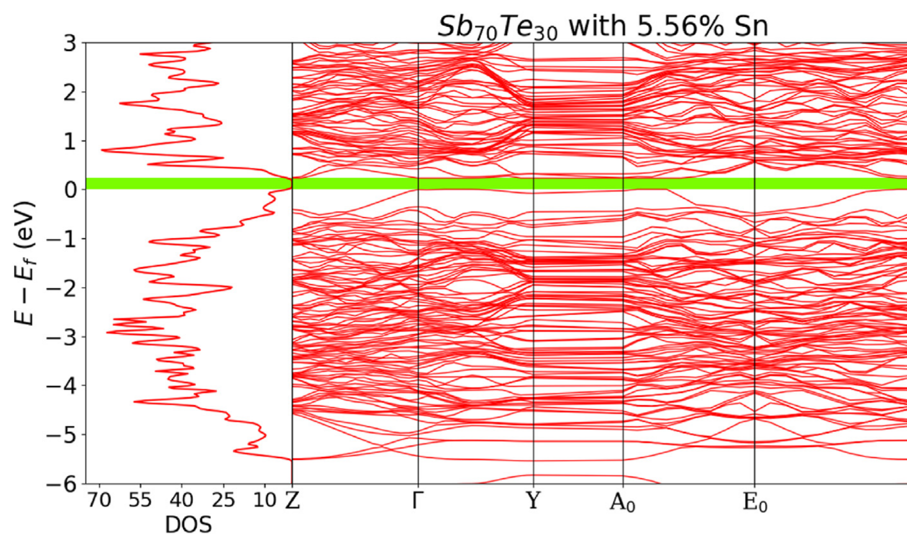

Fig. 11. Electronic band structure dispersion curves and DOS for the 5.56 at. % Sn-doped $Sb_{70}Te_{30}$, charged case. Electronic band gap is represented by green bar. (For interpretation of the references to color in this figure legend, the reader is referred to the Web version of this article.)

Declaration of competing interest

The authors declare that they have no known competing financial interests or personal relationships that could have appeared to influence the work reported in this paper.

Acknowledgments

This work has been partially supported by Peruilh scholarship (Facultad de Ingeniería-UBA), by the Universidad de Buenos Aires (UBACyT 20020170200377BA), ANPCYT (PICT 2015-1040) and CONICET (Argentina) PIP 0039. Calculations have been performed using computational resources of the "Proyecto Acelerado de Cálculo 2019" de la SNCAD-MINCyT, Centro de Computación de Alto Rendimiento (CECAR) FCEN-UBA - Argentina, CONICET (PIP0747, PIP0720), UNLP (Grant No. X845), UNNOBA (Grant SIB 0176/2017). D.E. acknowledges the financial support from the Spanish Ministerio de Ciencia, Innovación y Universidades, the Spanish Research Agency, the Generalitat Valenciana, and the European Fund for Regional Development under Grants No. MAT2016-75586-C4-1-P, PID2019-106383GB-C41, and No.Prometeo/2018/123 (EFIMAT). A.L. and D.E. would like to thank the Generalitat Valenciana for the Ph.D. fellowship GRISOLIAP/2019/025. The help of E.J. Di Liscia in Raman measurements is highly recognized.

References

[1] A. Lotnyk, M. Behrens, B. Rauschenbach, Phase change thin films for non-volatile memory applications, Nanoscale Adv. 1 (2019) 3836–3857, https://doi.org/10.1039/C9NA00366E.
[2] Xian-Bin Li, Nian-Ke Chen, Xue-Peng Wang, Hong-Bo Sun, Phase-change superlattice materials toward low power consumption and high density data storage: microscopic picture, working principles, and optimization, Adv. Funct. Mater. (2018) 1803380, https://doi.org/10.1002/adfm.201803380.
[3] P. Noé, Ch Vallée, F. Hippert, F. Fillot, J.Y. Raty, Phase-change materials for non-volatile memory devices: from technological challenges to materials science issues, Semicond. Sci. Technol. 33 (2018), 013002, https://doi.org/10.1088/1361-6641/aa7c25.
[4] G. Liu, L. Wu, M. Zhu, Z. Song, F. Rao, S. Song, Y. Cheng, The investigations of characteristics of Sb_2Te as a base phase-change material, Solid State Electron. 135 (2017) 31e36, https://doi.org/10.1016/j.sse.2017.06.004.
[5] M. Wuttig, N. Yamada, Phase-change materials for rewriteable data storage, Nat. Mater. 6 (2007) 824e832, https://doi.org/10.1038/nmat2009.
[6] J. Xu, F. Rao, Z. Song, M. Xia, C. Peng, Y. Gu, M. Zhu, L. Wu, B. Liu, S. Feng, High speed phase change memory based on SnTe-doped $Ge_2Sb_2Te_5$ material, Electrochem. Solid State Lett. 15 (3) (2012) H59eH61, https://doi.org/10.1149/2.006203esl.
[7] J.A. Rocca, V. Bilovol, D. Errandonea, A.V. Gil Rebaza, A.M. Mudarra Navarro, H.H. Medina Chanduví, L.A. Errico, B. Arcondo, M. Fontana, O. Cuellar Rodríguez, M.A. Ureña, Structural and Mössbauer study of $(Sb_{0.70}Te_{0.30})_{100-x}Sn_x$ alloys with x=0, 2.5, 5.0 and 7.5, J. Alloys Compd. 795 (2019) 27–33, https://doi.org/10.1016/j.jallcom.2019.04.214.
[8] M.A. Ureña, M. Fontana, B. Arcondo, M.T. Clavaguera-Mora, Crystallization processes of Ag-Ge-Se superionic glasses, J. Non-Cryst. Solids 320 (2003) 151–167, https://doi.org/10.1016/S0022-3093(03)00022-X.
[9] R. Martin, Electronic Structure: Basic Theory and Practical Methods, Cambridge University Press, USA, 2008.
[10] P. Giannozzi, O. Andreussi, T. Brumme, O. Bunau, M.B. Nardelli, M. Calandra, R. Car, C. Cavazzoni, D. Ceresoli, M. Cococcioni, N. Colonna, I. Carnimeo, A.D. Corso, S. de Gironcoli, P. Delugas, R. D Jr., A. Ferretti, A. Floris, G. Fratesi, G. Fugallo, R. Gebauer, U. Gerstmann, F. Giustino, T. Gorni, J. Jia, M. Kawamura, H.-Y. Ko, A. Kokalj, E. Kkbenli, M. Lazzeri, M. Marsili, N. Marzari, F. Mauri, N. Nguyen, H.-V. Nguyen, A.O. de-la Roza, L. Paulatto, S. Ponc, D. Rocca, R. Sabatini, B. Santra, M. Schlipf, A. Seitsonen, A. Smogunov, I. Timrov, T. Thonhauser, P. Umari, N. Vast, X. Wu, S. Baroni, Advanced capabilities for materials modeling with QUANTUM ESPRESSO, J. Phys. Condens. Matter 29 (2017), https://doi.org/10.1088/1361-648X/aa8f79.
[11] J. Perdew, K. Burke, M. Ernzerhof, Generalized gradient approximation made simple, Phys. Rev. Lett. 7 (1996) 3865–3868, https://doi.org/10.1103/PhysRevLett.77.3865.
[12] G. Prandini, A. Marrazzo, I. Castelli, N. Mounet, N. Marzari, Precision and efficiency in solid-state pseudopotential calculations, Computat. Mater. 4 (2018) 1e13, https://doi.org/10.1038/s41524-018-0127-2.
[13] S. Baroni, S. de Gironcoli, A. Dal Corso, P. Giannozzi, Phonons and related crystal properties from density-functional perturbation theory, Rev. Mod. Phys. 73 (2001) 515–562, https://doi.org/10.1103/RevModPhys.73.515.
[14] M. Lazzeri, M. Calandra, F. Mauri, Anharmonic phonon frequency shift in MgB2, Phys. Rev. B 68 (2003) 220509, https://doi.org/10.1103/PhysRevB.68.220509.
[15] P. Blaha, K. Schwarz, G.K.H. Madsen, D. Kvasnicka, J. Luitz, R. Laskowski, F. Tran, L.D. Marks, WIEN2k: an Augmented Plane Wave Plus Local Orbitals Program for Calculating Crystal Properties, Karlheinz Scwarz, Technische Universität Wien, Austria, 2018, ISBN 3-9501031-1-2.
[16] P. Blaha, K. Schwarz, F. Tran, R. Laskowski, G.K.H. Madsen, L.D. Marks, WIEN2k: an APW+lo program for calculating the properties of solids, J. Chem. Phys. 152 (2020), 074101, https://doi.org/10.1063/1.5143061.
[17] F. Tran, P. Blaha, Accurate band gaps of semiconductors and insulators with a semilocal exchange-correlation potential, Phys. Rev. Lett. 102 (2009) 226401, https://doi.org/10.1103/PhysRevLett.102.226401.
[18] D. Koller, F. Tran, P. Blaha, Improving the modified Becke-Johnson exchange potential, Phys. Rev. B 85 (2012) 155109, https://doi.org/10.1103/PhysRevB.85.155109.
[19] N. Yamada, T. Matsunaga, Structure of laser-crystallized $Ge_2Sb_{2+x}Te_5$ sputtered thin films for use in optical memory, J. Appl. Phys. 88 (2020) 7020, https://doi.org/10.1063/1.1314323.
[20] D.J. Wouters, R. Has beener, M. Wuttig, Phase-change and redox-based resistive switching memories, Proc. IEEE 103 (8) (2015) 1274–1288, https://doi.org/10.1109/JPROC.2015.2433311.
[21] Y.C. Her, Y.S. Hsu, Thickness dependence of crystallization and melting kinetics of eutectic $Sb_{70}Te_{30}$ phase change recording film, J. Non-Cryst. Solids 354 (27) (2008) 3129–3134, https://doi.org/10.1016/j.jnoncrysol.2008.01.021, 1.
[22] E. Prokhorov, A. Mendoza-Galván, J. González-Hernández, B. Chao, Effects of Ge addition on the optical and electrical properties of eutectic $Sb_{70}Te_{30}$ films, J. Non-Cryst. Solids 353 (2007) 1870–1874, https://doi.org/10.1016/j.jnoncrysol.2007.02.017.
[23] E. Prokhorov, J. González-Hernández, A. Mendoza-Galván, G. Trapaga, G. Luna-Bárcenas, Structural and electrical properties of germanium-doped $Sb_{70}Te_{30}$ eutectic thin films, J. Non-Cryst. Solids 357 (2011) 1610–1614, https://doi.org/10.1016/j.jnoncrysol.2009.05.072.
[24] G. Wang, X. Shen, Q. Nie, R.P. Wang, L. Wu, Y. Lu, S. Dai, T. Xu, Y. Chen, Improved phse-change characteristics of Zn-doped amorphous Sb7Te3 films for high-speed and low-power phase change memory, Appl. Phys. Lett. 103 (2013), 031914, https://doi.org/10.1063/1.4816062.
[25] H.-Y. Cheng, K.-F. Kao, C.-M. Lee, T.-S. Chin, Characteristics of GaeSbeTe films for phase-change memory, IEEE Trans. Magn. 43 (2) (2007) 927, https://doi.org/10.1109/TMAG.2006.888516.
[26] Y.S. Hsu, Y.C. Her, S.T. Cheng, S.Y. Tsai, Thermal- and laser-induced order-disorder switching os Ag-doped fast-growth Sb70Te30 phase-change recording films, Jpn. J. Appl. Phys. 46 (2007) 3945, https://doi.org/10.1143/JJAP.46.3945.
[27] H.Y. Cheng, K.F. Kao, C.A. Jong, C.J. Lan, T.S. Chin, Characteristics of Ga-Sb-Te films for phase-change memory, IEEE Trans. Magn. 43 (2007) 930–932, https://doi.org/10.1109/TMAG.2006.888516.
[28] S. Raoux, M. Salinga, J. Jordan-Sweet, A. Kellock, Effect of Al and Cu doping on the crystallization properties of the phase change materials SbTe and GeSb, J. Appl. Phys. 101 (2007), 044909, https://doi.org/10.1063/1.2654556.
[29] K. Tanaka, K. Shimakawa, Amorphous Chalcogenide Semiconductors and Related Materials, Springer, New York, 2011, p. 87.
[30] P. Villars, A. Prince, H. Okamoto, Handbook of Ternary Alloy Phase Diagrams, ASM International, 1995.
[31] M.A. Hakeem, D.E. Jackson, J.J. Hamlin, D. Errandonea, J.E. Proctor, M. Bettinelli, High pressure Raman, optical absorption, and resistivity study of $SrCrO_4$, Inorg. Chem. 57 (2018) 7550–7557, https://doi.org/10.1021/acs.inorgchem.8b00268.
[32] T. Marqueño, D. Errandonea, J. Pellicer-Porres, D. Martinez-Garcia, D. Santamaria-Pérez, A. Muñoz, P. Rodríguez-Hernández, A. Mujica, S. Radescu, S.N. Achary, C. Popescu, M. Bettinelli, High-pressure polymorphs of gadolinium orthovanadate: X-ray diffraction, Raman spectroscopy, and ab initio calculations, Phys. Rev. B 100 (2019), 064106, https://doi.org/10.1103/PhysRevB.100.064106.
[33] D. Errandonea, F.J. Manjón, A. Muñoz, P. Rodríguez-Hernández, V. Panchal, S.N. Achary, A.K. Tyagi, High-pressure polymorphs of $TbVO_4$: a Raman and *ab initio* study, J. Alloys Compd. 577 (2013) 327–335, https://doi.org/10.1016/j.jallcom.2013.06.008.
[34] M.N. Schneider, F. Fahrnbauer, T. Rosenthal, M. Doeblinger, C. Stiewe, O. Oeckler, Elemental distribution and thermoelectric properties of layered tellurides 39R-$M_{0.067}Sb_{0.667}Te_{0.266}$ (M=Ge, Sn), Chem. Eur J. 18 (4) (2012) 1209–1218, https://doi.org/10.1002/chem.201102331.
[35] L.A. Errico, G. Fabricius, M. Rentería, Metal impurities in an oxide: ab initio study of electronic and structural properties of Cd in rutile TiO2, Phys. Rev. B 67 (2003) 144104, https://doi.org/10.1103/PhysRevB.67.144104.
[36] R.F.W. Bader, Atoms in Molecules: A Quantum Theory, Oxford University Press, New York, 1994.
[37] M. Woda, Electrical Transport in Crystalline Phase Change Materials, Doctoral Thesis, Westfälischen Technischen Hochschule Aachen University, 2010, https://core.ac.uk/download/pdf/36448046.pdf.